Journal of Catalysis 268 (2009) 235–242

Contents lists available at ScienceDirect

Journal of Catalysis

journal homepage: www.elsevier.com/locate/jcat

Insights into the nature of iron-based Fischer–Tropsch catalysts from quasi in situ TEM-EELS and XRD

S. Janbroers [a,b,*], J.N. Louwen [a], H.W. Zandbergen [b], P.J. Kooyman [c,b]

[a] *Albemarle Catalysts B.V., Nieuwendammerkade 1-3, 1030 BE Amsterdam, The Netherlands*
[b] *Kavli Institute of Nanoscience, Delft University of Technology, Lorentzweg 1, 2628 CJ Delft, The Netherlands*
[c] *DelftChemTech, Delft University of Technology, Julianalaan 136, 2628 BL Delft, The Netherlands*

ARTICLE INFO

Article history:
Received 14 April 2009
Revised 21 September 2009
Accepted 24 September 2009
Available online 31 October 2009

Keywords:
TEM-EELS
XRD
Fischer–Tropsch
Iron carbide
Iron oxide
Oxidation
Passivation

ABSTRACT

Although assumed to be iron carbide, the active phase of iron-based Fischer–Tropsch catalysts remains unresolved. An important issue is the air-sensitivity of the active catalysts. In this model study, exposure to air is prevented completely by performing both XRD and TEM-EELS in quasi in situ mode. Starting from hematite precursors, carburized catalysts contain mainly iron carbide of as yet unknown structure and some magnetite. The latter is not covered with amorphous carbon, whereas the carbide is covered. Carburized catalysts change significantly upon (controlled or uncontrolled) air exposure. During re-oxidation carbon is freed and deposited as a separate amorphous phase. When studying iron-based Fischer–Tropsch catalysts, exposure to air should be avoided completely.

1. Introduction

The Fischer–Tropsch process is the production of a high quality, synthetic petroleum substitute by coupling carbon monoxide and hydrogen ‘synthesis gas’ (syngas) to hydrocarbons using a catalyst. The (simplified) reaction can be expressed as $n\text{CO} + (2n+1)\text{H}_2 \rightarrow \text{C}_n\text{H}_{2n+2} + n\text{H}_2\text{O}$. The catalysts are usually based on cobalt or iron [1], each having its own advantages and disadvantages [2]. In this study, we focus on iron-based catalysts. The syngas is often derived from natural gas (e.g. by steam reforming) or from coal gasification. Coal is an interesting raw material since very large reserves still remain [3]. It can be used as an interim fuel source when conventional oil is becoming scarce. Syngas can also be obtained by gasification of bio-mass, making it a truly sustainable alternative.

The best catalytic performance is often obtained by starting from iron oxide precursors prepared via precipitation [4–8] to which different promoters are added. The most important promoters include potassium and copper [4,9–15]. As the activation step takes place inside the reactor (in situ at high temperature and pressure), studying this activation process is not trivial. As a result, the identity of the real active phase is still unknown. It is believed that iron carbides are the key components, being five times more active than iron oxides [16,17]. Free carbon is thought to play an essential part in the catalytic process [18–21]. It was also suggested that part of this carbon could have been formed by air exposure during sample handling prior to analysis [22].

It is known that many published ex situ characterization studies are unsuccessful [23] since the samples are sensitive to air exposure. During contact with ambient air, the catalyst is oxidized extensively and no information can be obtained anymore on the actual working catalyst. It was suggested that the best one can do is to perform a passivation, which is to expose the specimen to air under controlled conditions in order to prevent excessive oxidation. This method has been used in detailed TEM-EELS characterization studies [22,24]. Nevertheless, any oxidation (controlled or not) inevitably changes the active state of the catalyst surface under study.

To overcome this problem, (quasi) in situ measurements can be performed, preventing exposure to air. This has been done extensively using X-Ray Diffraction (XRD) and Mössbauer spectroscopy [16,25–27]. However, these bulk techniques lack spatial resolution and do not necessarily give information on the catalyst surface (which is where the catalytic reactions take place). Recently, a study using in situ transmission X-ray microscopy showed a large improvement in this respect, achieving a spatial resolution of several tens of nm [28]. A technique that provides very high spatial resolutions (in the nm range) is HRTEM or STEM

---

* Corresponding author. Address: Albemarle Catalysts B.V., Nieuwendammerkade 1-3, 1030 BE Amsterdam, The Netherlands.
E-mail address: Stephan.Janbroers@Albemarle.com (S. Janbroers).

0021-9517/$ - see front matter © 2009 Elsevier Inc. All rights reserved.
doi:10.1016/j.jcat.2009.09.021

in combination with EELS [29]. However, the activated or used catalysts have to be transferred to the electron microscope without exposure to air.

In our model study, the samples are mounted on a gold–palladium microgrid supported on a gold grid [30], all in an Ar glove box. The samples are transferred to the microscope in a special protective atmosphere transfer sample holder under exclusion of air [31]. Once the closed holder is inside the microscope, it is opened again and the sample can be studied. Using this equipment, no passivation is required and the catalyst surface can be studied without having been exposed to air.

We study carburized iron catalysts using quasi in situ XRD, TEM, and EELS. We report the effects of both controlled passivation and uncontrolled exposure to air. Note that our carburized samples represent catalysts after CO activation at atmospheric pressure only. Depending on the reaction conditions, the catalyst is again prone to changes during prolonged FT reaction [11]. This will be the subject of a subsequent study.

2. Experimental

2.1. Catalyst preparation

A first sample was prepared by precipitating iron nitrate with ammonia. While stirring at 70 °C, 11.2 kg 4 N ammonia was added to a solution of 5.06 kg $Fe(NO_3)_3{\cdot}9H_2O$ and 14.6 kg water until the pH reached 7.4. After filtration and subsequent washing with demineralized water, a 5 wt% slurry was prepared by adding additional water. To this slurry, K_2CO_3 and $Cu(NO_3)_2{\cdot}3H_2O$ were added to obtain a final catalyst loading of 0.8 wt% K_2O and 0.8 wt% CuO. The slurry was spray-dried using a conventional spray-drier (Type Niro SD-6.3-R equipped with a Niro FU11 rotary atomizer). Settings: rotary speed = 12,600 rpm, inlet temperature = 400 °C, outlet temperature = 140 °C. Calcination was performed using a Carbolite HTR 11/150 rotary furnace (ramp = 2°/min, final temperature = 300 °C, dwell = 4 h).

A second sample was prepared in a similar way with the exception that no potassium or copper was added before spray-drying. Instead, the equivalents of 0.8 wt% K_2O and 0.8 wt% CuO were added after spray-drying via a two-step incipient wetness impregnation using a solution of K_2CO_3 and $Cu(NO_3)_2{\cdot}3H_2O$, respectively. Each impregnation was followed by a drying and calcination step (drying: overnight at 120 °C, calcination: ramp = 5°/min, final temperature = 300 °C, dwell = 4 h).

A hematite reference was prepared by calcining the spray-dried intermediate twice at 1000 °C (ramp = 5°/min, dwell = 10 h), cooling to room temperature after each calcination step.

2.2. Carburization experiments

Catalyst activation was mimicked using a specially designed set-up consisting of a calibrated flow meter, quartz U-tube, and an oven. 350 mg Iron oxide catalyst precursor was sandwiched in between quartz-wool at the bottom of the U-tube.

The carburization procedure was performed at atmospheric pressure:

- 2 °C/min to 150 °C in helium (10 ml/min);
- switch to carbon monoxide (5 ml/min);
- 2 °C/min to 270 °C;
- dwell for 24 h;
- switch to helium (10 ml/min);
- cool down to room temperature;
- the U-tube was closed and the sample was transferred to a glove box.

2.3. Small scale oxidation/passivation experiments

The effects of oxidation were investigated using two different methods:

1. An uncontrolled exposure to air by simply taking out the TEM holder from the microscope after studying the carburized samples. After 2 min of exposure, the TEM holder was reinserted into the microscope.
2. A controlled exposure to air (passivation) as indicated by Shroff et al. [23]. We used a vacuum chamber into which we could insert the (closed) protective atmosphere transfer TEM holder. By lowering the pressure to 40 mbar using a turbo pump, an atmosphere of 0.8% O_2 was created. The TEM holder was opened once the chamber pressure was stable. The samples were then exposed for 30 min at room temperature.

Note that we closed the holder again during transport back to the TEM, so the only exposure to oxygen was inside the passivation set-up.

By performing these treatments on the catalyst dispersed on the TEM grid, we were able to study exactly the same areas of the samples before and after oxidation.

2.4. X-Ray Diffraction (XRD)

XRD was performed using a Bruker D8 diffractometer equipped with a Cu Kα source. Variable (θ-compensating) anti-scatter and divergence slits were used. Rietveld refinement was performed using the GSAS software package [32].

The carburized samples were measured quasi in situ under nitrogen using a special dome (Bruker AB100B36). Unfortunately, the subsequent passivation of these samples proceeded in a less controlled manner than originally planned. TEM-EELS analysis of these samples (not shown) shows similar results compared to other properly passivated samples, so we consider these samples as passivated properly.

2.5. TEM-EELS

The samples were examined using a FEI Tecnai F20 TEM equipped with a Field Emission Gun (FEG), a Gatan 4k × 4k ultrascan camera, and Gatan Image Filter (GIF), operated at 200 kV. The EELS edges were quantified by integration of the peak areas as described by Mitchell [33]. We used the peak areas to determine the valence states of the iron species and to calculate iron/oxygen ratios, which is a semi-quantitative way to determine the relative degrees of oxidation. By performing Fourier Transforms using Digital Micrograph 3.1™, we were able to determine the lattice spacings. Special carbon-free TEM grids were used to minimize interference [30].

3. Results and discussion

3.1. The oxidic catalyst precursors

XRD results of the calcined oxidic precursors prove that hematite (Fe_2O_3) is the main crystalline phase present (not shown). TEM images show spherical/elliptical crystallites with sizes of about 5–50 nm. At higher magnification lattice spacings can be observed, consistent with the d-spacings of hematite [JCPDS#33664]. By calculating the L_3/L_2 ratios (area/area) from EELS data (not shown), the oxidation state of the iron can be determined [24]. We found L_3/L_2 ratios of 5.7, 5.8, and 5.4 for both samples and the hematite reference, respectively. This proves that the iron in all samples is Fe(III), consistent with the hematite structure.

3.2. The carburized samples

A typical XRD pattern of a carburized sample is shown in Fig. 1a. (black line) together with a scan of the sample after exposure to oxygen (gray line). No hematite is found anymore. Magnetite (Fe_3O_4) is clearly present in both samples, albeit as a minor phase. The scan is dominated by signals from a poorly crystalline iron carbide phase characterized by diffraction lines at 39.2°, 41.0°, 43.5°,

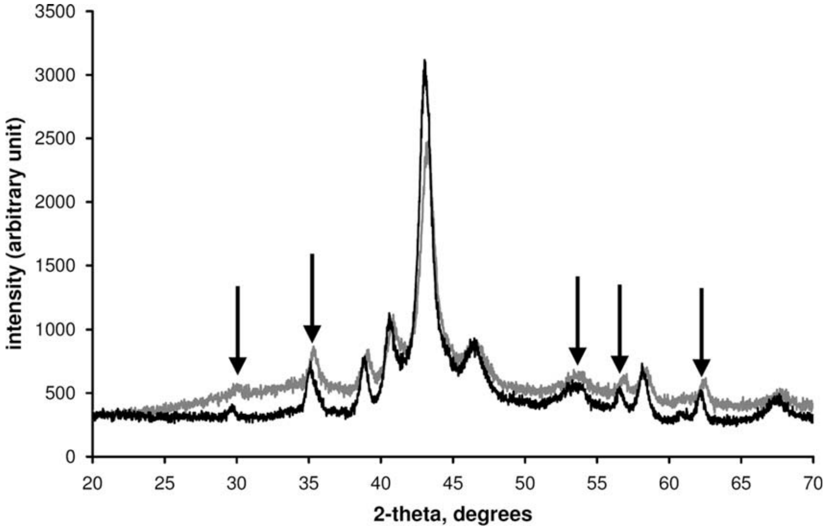

Fig. 1. Powder XRD patterns after carburization (black line) and passivation (gray line). Arrows indicate diffraction lines due to magnetite.

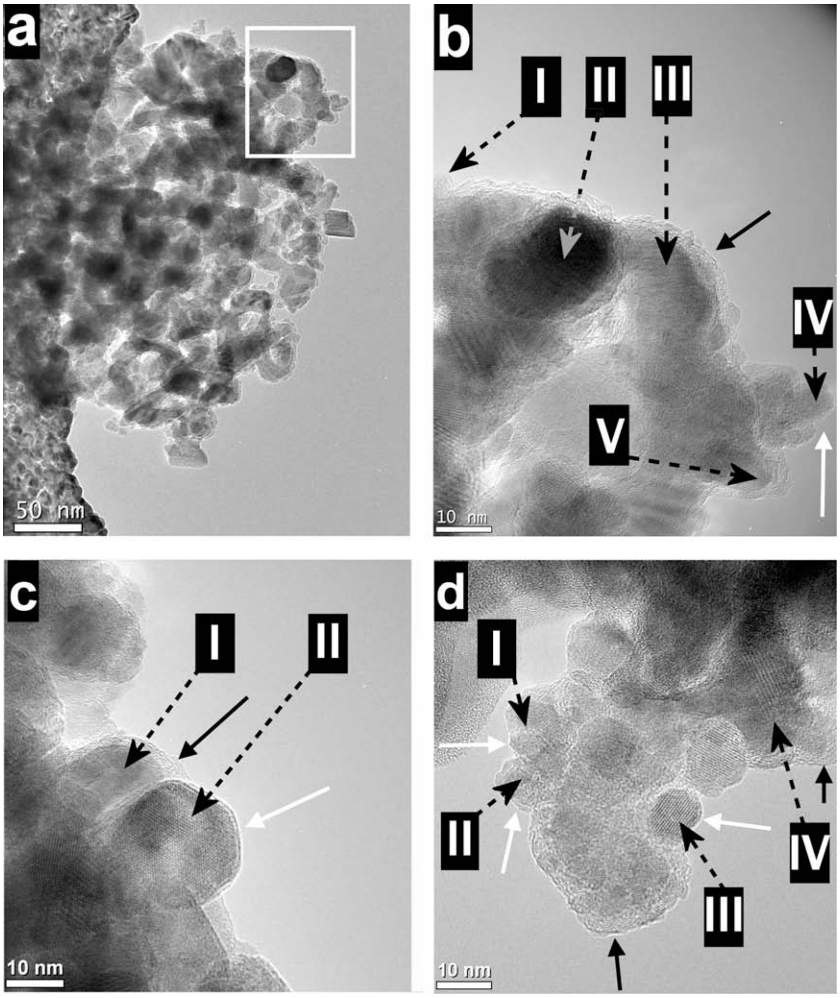

Fig. 2. TEM images of carburized samples. The area highlighted in (a) is magnified in (b). The white arrows show the clean iron oxide surface; the black arrows show carbon layers; and the dotted arrows indicate the areas used for FFT analysis.

46.8°, 58.5°, and 67.7° 2θ (d-spacings of 2.30, 2.20, 2.08, 1.94, 1.58, and 1.38 Å, respectively). Upon oxidation this phase decreases in intensity, while the background is enhanced by a substantial amount of amorphous halo.

Crystal structures are known for ε'-$Fe_{2.2}C$, χ-Fe_5C_2, ε-Fe_3C, and Fe_7C_3 [34], η-Fe_2C [35], θ-Fe_3C [36], Fe_4C [37] . However, none of these structures yield a simulated pattern corresponding completely to the XRD pattern obtained here. Datye et al. published a pattern that appears to be similar to our data [38], explaining the differences as due to severely faulted χ-Fe_5C_2. Likewise, Jin [39] provides powder XRD patterns of iron carbides in which this phase appears to be present (among other phases). He too suggests that the signal is due to χ-Fe_5C_2. In our case Rietveld refinement, using magnetite and χ-Fe_5C_2 as phases for the simulation, could not give a satisfactory match. An unrealistic shape of the fitted background is obtained due to several intense lines of χ-Fe_5C_2 inevitably becoming very broad to match the observed scan, which is necessarily compensated for by the fitted background.

Different iron carbides can be formed with varying iron to carbon ratios [40,41], its formation depending on both the nature of the catalyst and the reaction conditions [18]. Based on the data we have, no conclusions can be drawn about the structure we obtained under our (atmospheric pressure) activation condition. We hope to resolve this matter by means of electron diffraction in the near future.

Typical TEM images of the carburized samples are shown in Fig. 2a–d. Note that the specimens were carefully transported under inert to avoid oxidation. In addition we adapted methods to ensure that no external contaminations (including carbon pick-up) occur [30]. The morphology of the oxidic precursor changed completely upon carburization. The spherical/elliptical crystallites become much more irregularly shaped and different crystalline phases are observed. Also, small amounts of graphitic and amorphous carbon are detected. By performing Fourier Transforms of the crystalline areas we are able to distinguish between iron oxide and iron carbide species. The areas used for these calculations are indicated I–V in each image; the results are shown in Table 1. Spacings around 2.1 Å cannot unambiguously be assigned to magnetite (2.10 Å) or iron carbide (2.08 Å). In some cases, the spacings between 3.9 and 4.1 Å are found which we cannot yet assign to a specific phase. A detailed electron diffraction study will be undertaken in the near future to identify this unknown phase. EELS data (not shown) confirm the XRD findings. The L_3/L_2 ratios (area/area) decrease from about 5.8 to 2.9, showing the iron species to be reduced to either metallic iron or iron carbides.

Different carbon layers are highlighted with black arrows in Fig. 2b–d. The white arrows show the magnetite crystallites without any carbon layers. Our data show that amorphous carbon is present after the carburization but that these deposits reside on the carbide phases and not on the magnetite. This is consistent with the work of Shroff et al. [42] although no explanation was given at the time. Bukur et al. [43] assumed that a Boudouard reaction is responsible for the carbon deposits while more recently, Jin et al. [24] suggested that an excess of carbon from the iron-carbide phases can precipitate on the particle surface during cooling of the sample prior to analyses. In other words, the carbon layers may not even be present under reaction conditions. Overall, the exact mechanism is still unclear but we hope to elucidate this issue in

Table 1
FFT results and phase assignments.

Corresponding figure	Area	Spacing (Å)	Corresponding °2θ	Assignment based on XRD data	Carbon layer present
3b	1	2.50	35.3	Magnetite	No
	II	2.33	38.0	Iron carbide	Yes
	II	2.27	39.0	Iron carbide	Yes
	II	2.36	37.5	Iron carbide	Yes
	III	2.05	43.2	Iron carbide/magnetite	Yes
	III	2.06	42.8	Iron carbide/magnetite	Yes
	III	1.97	44.8	Iron carbide	Yes
	III	3.94	22.5	Unknown	Yes
	IV	2.94	30.1	Magnetite	No
	V	2.06	42.9	Magnetite/iron carbide	Yes
	V	1.96	45.0	Iron carbide	Yes
	V	2.09	42.3	Iron carbide/magnetite	Yes
3c	1	2.13	41.4	Magnetite/iron carbide	Yes
	1	2.48	35.7	Magnetite	Yes
	1	2.21	40.0	Iron carbide	Yes
	1	1.91	46.3	Iron carbide	Yes
	1	2.13	41.4	Magnetite/iron carbide	Yes
	II	2.13	41.5	Magnetite/iron carbide	No
	II	3.98	22.2	Unknown	No
	II	2.44	36.2	Magnetite	No
	II	2.80	31.5	Magnetite	No
	II	2.47	35.8	Magnetite	No
	II	4.12	21.5	Unknown	No
3d	1	2.44	36.2	Magnetite	No
	II	2.87	30.8	Magnetite	No
	III	2.95	30.0	Magnetite	No
	III	2.52	35.1	Magnetite	No
	III	2.06	42.9	Magnetite	No
	III	2.47	35.8	Magnetite	No
	III	4.83	18.3	Magnetite	No
	IV	1.90	46.5	Iron carbide	Yes
	IV	2.15	41.0	Iron carbide	Yes
	IV	2.14	41.2	Iron carbide	Yes
7c		2.89	30.5	Magnetite	No
7d		1.47	60.1	Magnetite	Yes
		2.89	30.6	Magnetite	Yes

the near future by performing in situ TEM-EELS carburization studies.

3.3. Uncontrolled oxidation

In 1996, Shroff published a paper entitled *'The importance of passivation in the study of iron Fischer–Tropsch catalysts'* [23]. It stated that uncontrolled exposure of activated iron-based FT catalysts should be avoided. Subsequently, several other research groups have adapted passivation procedures, such as Mansker et al. [44]. Our data confirm the detrimental effect of uncontrolled exposure to air, although we observe similar detrimental phenomena after passivation (vide infra).

We transferred a carburized catalyst under inert as explained in Section 3.2 (Fig. 3a). Following detailed TEM-EELS study, this catalyst was exposed to oxidation in an uncontrolled manner while present on the TEM grid (Fig. 3b). The data (of the same area of the catalyst) show that the morphology changed completely. Many crystallites disappear after exposure to air and regroup into completely different particles, indicating that the oxidation is not limited to a surface layer. EELS data of the same area are presented in Fig. 4a–c. The edge intensities are normalized to the total iron edge area, allowing quantitative comparison. Fig. 4a shows that the iron L_3/L_2 ratio (area/area) increased from 2.9 to 3.8; and Fig. 4b shows that the Fe/O ratio (area/area) decreased from 11.3 to 7.2. Both observations prove that the sample has been oxidized.

The carbon K-edges (Fig. 4c) show a change in the π^* to σ^* ratio after oxidation. The higher σ^* peak indicates a more amorphous character, similar to the amorphous carbon reference. The increase in total peak area after exposure to air suggests that the relative amount of carbon has increased. This increase is caused by mobile carbon species freed from all over the sample, migrating to the area under observation and decomposing there under the electron beam, forming amorphous carbon. Although the exact nature of the mobile carbon species is unclear, this effect is consistent for all re-oxidized samples described in this paper (including the passivated ones). Due to the instability of the samples after exposure to air, accurate measurements become increasingly difficult. Since the species are mobile and decompose under the electron beam, the carbon build-up during the TEM-EELS measurements is considerable (not shown). We confirmed that the TEM grids themselves show no contamination at all even after prolonged exposure to ambient air [30], making it highly unlikely that this contamination is introduced by adsorption of hydrocarbons during air exposure. To exclude other side effects, we also measured the areas that had not been exposed to the electron beam prior to exposure to air, obtaining identical results. In other words, the carbon build-up we observed is not induced by the electron beam before air

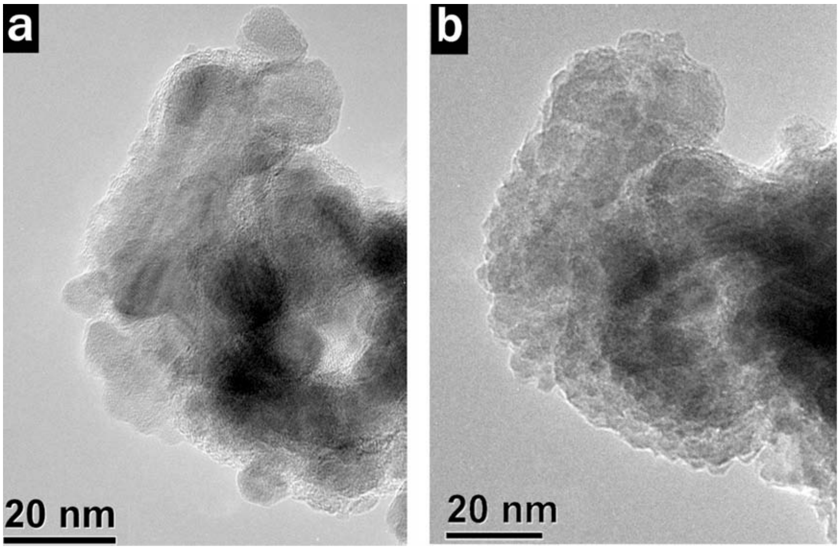

Fig. 3. TEM images of the same area showing a carburized sample before (a) and after (b) uncontrolled oxidation.

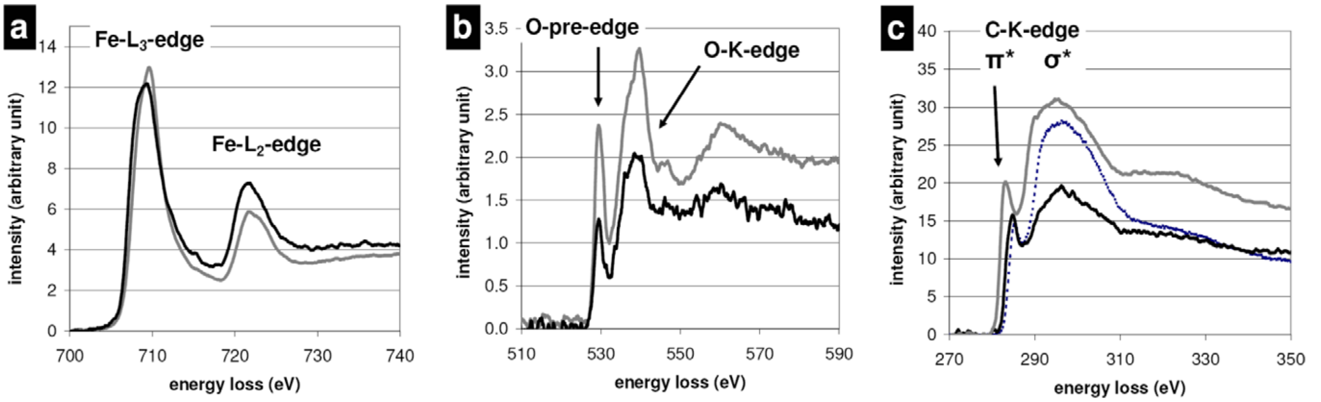

Fig. 4. EEL spectra showing the iron, oxygen, and carbon edges before (black) and after (gray) uncontrolled oxidation. (c) Shows an amorphous carbon reference (dotted line; for illustrative purposes only).

exposure. Therefore, these mobile carbon species are formed during exposure to air. The carbon is freed from the iron–carbon species as was proposed by Graham et al. [22]. The exact nature of these mobile carbon species is not yet known but will be studied in more detail.

3.4. The effect of passivation

As explained previously, iron oxide particles are still observed in carburized samples, without any carbon layers present at their surface. Passivation induces changes, although the effects are more subtle than after uncontrolled exposure to air. Apart from an overall thickening of the carbon layers that were already present before exposure, all iron oxide particles are now also covered with carbon layers (compare Fig. 5a with b and c with d). This is especially clear at higher magnification as shown in Fig. 5a, b and Table 1 (summarizing the corresponding FFT results).

EELS data show that the carbides have been oxidized after passivation. Fig. 6a–c shows the iron-, oxygen- and carbon edges of the particle indicated by a circle shown in Fig. 5c and d. The L_3/L_2 ratio (area/area) of the iron edge has increased from 2.6 to 4.3 after passivation. In addition, the Fe/O ratio (area/area) changed from 11.7 to 0.6.

Before passivation, the carbon K-edge (Fig. 6c; black line) shows a relatively high π^*-line compared to the σ^*-line. This is a confirmation of the carbidic character. The shape of the edge suggests that some graphitic carbon might be present as well. This effect has been described before [24]. After passivation, the amount of carbon has increased considerably as explained before. Mobile carbon is freed from the iron carbide phase and the crystallinity of the carbon decreases.

Amorphous deposits on the iron species have been described extensively. It is undisputed that such layers can be formed during carburization [42,43,45] but also during the Fischer–Tropsch synthesis (related to deactivation) [18]. However, Graham et al. [22] stated that passivation of iron carbide could also result in the deposition of carbon if the only reaction with oxygen was to produce Fe_3O_4 and Fe_2O_3. In other words, they suggest that the layered carbon that is found on iron carbides as well as iron oxides might partially be an artifact of exposure to air. Our data confirm these suggestions.

Our findings agree with those of Shroff et al. [42] who found that carbide particles were covered with a surface film of carbon while the magnetite surface was clean. He found that these surface films are formed during a Fischer–Tropsch reaction. However, we observed these carbon layers already directly after the CO activation procedure so without the need to passivate or perform any Fischer–Tropsch reaction. This contradiction might be explained by the much shorter activation times applied by Shroff; viz. 2 h compared to 24 h for our samples. In fact, Shroff hardly found any carbide formation after 2 h of CO activation. It seems likely that the catalyst was still being carburized while exposed to a

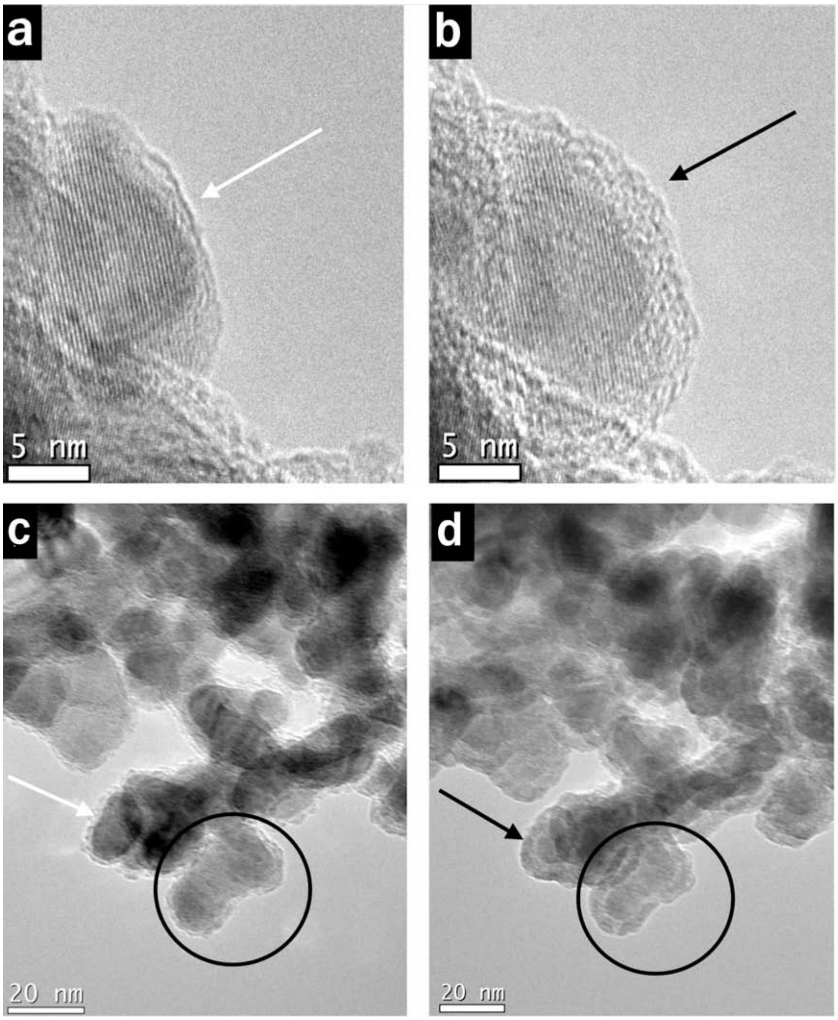

Fig. 5. TEM images before (a, c) and after (b, d) passivation. Changes are indicated with white and black arrows before and after passivation, respectively.

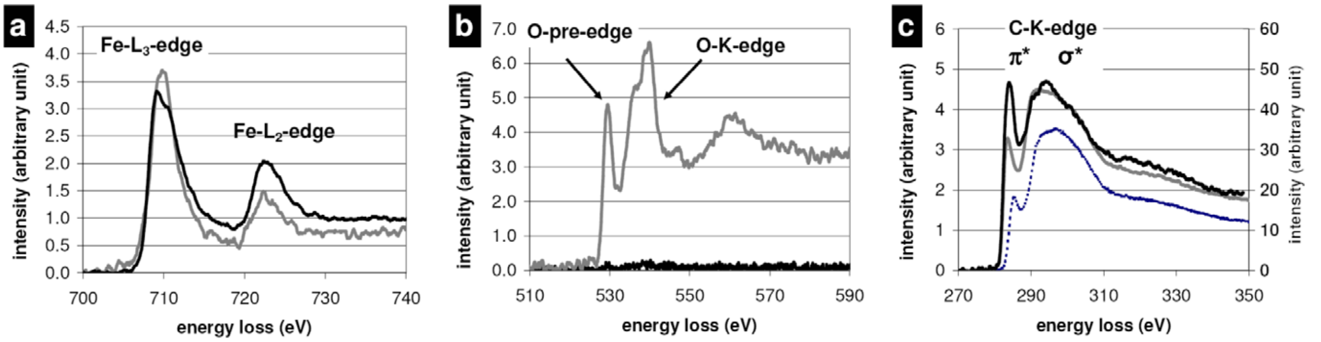

Fig. 6. EEL spectra showing the iron, oxygen, and carbon edges before (black) and after passivation (gray). 6c also shows an amorphous carbon reference (dotted line; for illustrative purposes only).

syngas mixture, and the carbon deposits were formed via the Boudouard reaction.

Note that we see a substantial increase in carbon layer thickness after passivation. It is difficult to ascertain the exact catalyst surface from published data obtained for samples that have been exposed to air.

4. Conclusions

Carburization of iron Fischer–Tropsch catalysts in CO yields a mixture of different phases. XRD and TEM-EELS show that the precursor hematite is reduced to magnetite and iron carbide. The reduction of iron is clearly seen from the lower L_3/L_2 edge ratio (about 3.0 for iron carbide compared to 5.4 for hematite and magnetite). XRD shows mainly iron carbide with an unknown structure to be present next to magnetite. TEM results show that after carburization carbon layers are present but reside predominantly on iron-carbide species and not on iron oxide species.

Exposure to air leads to re-oxidation of the iron carbides. This is evident from the increase in EELS L_3/L_2 iron edge ratios and the decrease of the total iron to oxygen ratio. After exposure to air, the iron oxide species are covered in amorphous carbon. We believe that during re-oxidation, carbon is freed from its solid solution in iron or iron carbide and deposited as a separate amorphous phase. Additional research is required to determine the exact nature of these mobile carbon species. Nevertheless, our data show that the carbon surface layers can change, or even form, during exposure to air.

Overall, activated iron-based Fischer–Tropsch catalysts are very air-sensitive. Even after careful passivation the catalyst surface changes significantly and does not represent the actual catalyst surface anymore. When studying these catalysts, any exposure to air should be avoided.

Acknowledgments

We would like to thank Bert Klaver, Robert Jonker, Ronald Huiberts, and Leo van den Enden of Albemarle Catalysts B.V. (Nieuwendammerkade 1-3, 1030 BE, Amsterdam, The Netherlands) for their help with the catalyst preparation and carburization experiments. The help of Frans Tichelaar of Kavli Institute of Nanoscience (Delft University of Technology, Lorentzweg 1, 2628 CJ Delft, The Netherlands) at the TEM is highly appreciated. We are grateful to Frank Vergeer, Frank Geurts, and Rob van Puijenbroek of Akzo Nobel Chemicals (Velperweg 76, 6824 BM, Arnhem, The Netherlands) for their help with the XRD analysis. Leon van den Oetelaar is acknowledged for constructive criticism and fruitful discussions concerning Fischer–Tropsch catalysis.

NWO and 'Platform Beta techniek' are acknowledged for their financial support of this Casimir project.

References

[1] H. Pichler, in: W. Frankenburg, V. Komarewsky, E. Rideal (Eds.), Advances in Catalysis, vol. 4, Academic Press, New York, 1952, p. 271.
[2] A.A. Adeyiga, Development of Attrition Resistant Iron-Based Fischer–Tropsch Catalysts, Grant No.: DE-FG26-99FT 40619 for US Department of Energy, Grant No.: DE-FG26, 2003.
[3] G. Van der Laan, Kinetics, Selectivity and Scale Up of the Fischer–Tropsch Synthesis, University of Groningen, 1999.
[4] M.E. Dry, Catal. Sci. Technol. 1 (1981) 159.
[5] R.B. Anderson, The Fischer–Tropsch Synthesis, vol. 630-08-0, Academic Press, Florida, 1984.
[6] R.A. Diffenbach, D.J. Fauth, J. Catal. 100 (1986) 466.
[7] T.R. Motjope, H.T. Dlamini, H. Pollak, N.J. Coville, Hyperfine Interact. 120/121 (1999) 763.
[8] T.R. Motjope, H.T. Dlamini, G.R. Hearne, N.J. Coville, Catal. Today 71 (2002) 335.
[9] S. Li, G.D. Meitzner, E. Iglesia, J. Phys. Chem. B 105 (2001) 5743.
[10] R.A. Dictor, A.T. Bell, J. Catal. 97 (1986) 121.
[11] K.R.P.M. Rao, F.E. Huggins, G.P. Huffman, R.J. Gormley, R.J. O'Brien, B.H. Davis, Energy Fuels 10 (1996) 546.
[12] A.P. Raje, R.J. O'Brien, B.H. Davis, J. Catal. 180 (1998) 36.
[13] M. Luo, R.J. O'Brien, S. Bao, B.H. Davis, Appl. Catal. A 239 (2003) 111.
[14] Y. Yang, H.-W. Xiang, Y.-Y. Xu, L. Bai, Y.-W. Li, Appl. Catal. A 266 (2004) 181.
[15] R.J. O'Brien, B.H. Davis, Catal. Lett. 94 (2004) 1.
[16] B.H. Davis, Catal. Today 84 (2003) 83.
[17] Y. Zhang, N. Sirimanothan, R.J. O'Brien, H.H. Hamdeh, B.H. Davis, Stud. Surf. Sci. Catal. 139 (2001) 125.
[18] J.W. Niemantsverdriet, A.M. Van der Kraan, W.L. Van Dijk, H.S. Van der Baan, J. Phys. Chem. 84 (1980) 3363.
[19] J.P. Reymond, P. Meriaudeau, S.J. Teichner, J. Catal. 75 (1982) 39.
[20] D.B. Bukur, X. Lang, Y. Ding, Appl. Catal. A 186 (1999) 255.
[21] G. Bian, A. Oonuki, Y. Kobayashi, N. Koizumi, M. Yamada, Appl. Catal. A 219 (2001) 13.
[22] U.M. Graham, A. Dozier, R. Srinivasan, M. Thomas, B.H. Davis, Prepr. – Am. Chem. Soc., Div. Pet. Chem. 50 (2005) 178.
[23] M.D. Shroff, A.K. Datye, Catal. Lett. 37 (1996) 101.
[24] Y. Jin, H. Xu, A.K. Datye, Microsc. Microanal. 12 (2006) 124.
[25] H. Jung, W.J. Thomson, J. Catal. 134 (1992) 654.
[26] H. Jung, W.J. Thomson, J. Catal. 139 (1993) 375.
[27] S. Li, R.J. O'Brien, G.D. Meitzner, H. Hamdeh, B.H. Davis, E. Iglesia, Appl. Catal. A 219 (2001) 215.
[28] E. de Smit, I. Swart, J.F. Creemer, G.H. Hoveling, M.K. Gilles, T. Tyliszczak, P.J. Kooyman, H.W. Zandbergen, C. Morin, B.M. Weckhuysen, F.M. de Groot, Nature (London, UK) 456 (2008) 222.
[29] S. Lazar, G.A. Botton, M.-Y. Wu, F.D. Tichelaar, H.W. Zandbergen, Ultramicroscopy 96 (2003) 535.
[30] S. Janbroers, T.d. Kruijff, Q. Xu, P.J. Kooyman, H.W. Zandbergen, Ultramicroscopy 109 (2009) 1105.
[31] H.W. Zandbergen, P.J. Kooyman, A.D. Van Langeveld, Electron microscopy 1998, in: Proceedings ICEM 14, .vol. II, 1998, p. 491.
[32] A.C. Larson, R.B. Von Dreele, General Structure Analysis System (GSAS), Los Alamos National Laboratory, Report LAUR 86-748, 2000.
[33] D.R.G. Mitchell, Measure EELS Peak Intensities script version 2.1, 2006. <http://www.felmi-zfe.tugraz.at/dm_scripts/>
[34] K.M. Krishnan, Ultramicroscopy 32 (1990) 309.
[35] Y. Hirotsu, S. Nagakura, Acta Metall. 20 (1972) 645.
[36] D. Fruchart, P. Chaudouet, R. Fruchart, A. Rouault, J. Senateur, J. Solid State Chem. 51 (1984) 246.

[37] Z.G. Pinsker, S.V. Kaverin, Ref. Kristallogr. 1 (1956) 66.
[38] A.K. Datye, Y. Jin, L. Mansker, R.T. Motjope, T.H. Dlamini, N.J. Coville, Stud. Surf. Sci. Catal. 130B (2000) 1139.
[39] Y. Jin, Phase transformation of iron-based catalysts for Fischer–Tropsch synthesis, University of New Mexico, USA, 1999.
[40] G. Le Caer, J.M. Dubois, M. Pijolat, V. Perrichon, P. Bussiere, J. Phys. Chem. 86 (1982) 4799.
[41] G. Le Caer, Bauer-Grosse, Mater. Sci. Eng. 97 (1988) 273.
[42] M.D. Shroff, D.S. Kalakkad, K.E. Coulter, S.D. Koehler, M.S. Harrington, N.B. Jackson, A.G. Sault, A.K. Datye, J. Catal. 156 (1995) 185.
[43] D.B. Bukur, K. Okabe, M.P. Rosynek, C. Li, D. Wang, K.R.P.M. Rao, G.P. Huffman, J. Catal. 155 (1995) 353.
[44] L.D. Mansker, Y. Jin, D.B. Bukur, A.K. Datye, Appl. Catal. 186 (1999) 277.
[45] Y. Jin, A.K. Datye, J. Catal. 196 (2000) 8.